



http://pubs.acs.org/journal/acsodf Article

Strain-Driven In-plane Ordering in Vertically Aligned ZnO-Au Nanocomposites with Highly Correlated Metamaterial Properties

Robynne L. Paldi, Xing Sun, Xuejing Wang, Xinghang Zhang, and Haiyan Wang*



Cite This: ACS Omega 2020, 5, 2234-2241



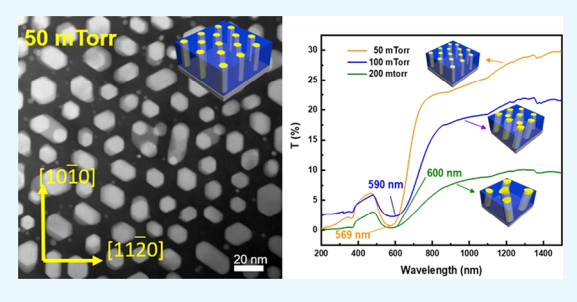
ACCESS

Metrics & More

Article Recommendations

Supporting Information

ABSTRACT: Hyperbolic metamaterials demonstrate exotic optical properties that are poised to find applications in subdiffraction imaging and hyperlenses. Key challenges remain for practical applications, such as high energy losses and lack of hyperbolic properties in shorter wavelengths. In this work, a new oxide—metal (ZnO—Au) hybrid-material system in the vertically aligned nanocomposite thin-film form has been demonstrated with very promising in-plane two-phase ordering using a one-step growth method. Au nanopillars grow epitaxially in the ZnO matrix, and the pillar morphology, orientation, and quasi-hexagonal in-plane ordering are found to be effectively tuned by the growth parameters. Strong surface plasmon



resonance has been observed in the hybrid system in the UV-vis range, and highly anisotropic dielectric properties have resulted with much broader and tunable hyperbolic wavelength regimes. The observed strain-driven two-phase in-plane ordering and its novel tunable hyperbolic metamaterial properties all demonstrate strong potential for future oxide-metal hybrid-material design toward future integrated hybrid photonics.

■ INTRODUCTION

Optical metamaterials with epsilon near-zero (ENZ) permittivity and hyperbolic dispersion can be created in nanostructures that consist of periodic arrangements of negative permittivity. The periodic nature of these structures creates photonic band gaps in which certain wavelengths of electromagnetic radiation are not permitted to propagate within the material. One way to achieve this structure is through directly embedding arrays of metallic nanowires into a dielectric medium, which is expected to create ENZ permittivity^{1,2} and lead to hyperbolic dispersion.^{3,4} The exciting realization of ENZ in the visible range could lead to exotic functionalities including light squeezing by subwavelength waveguides, 5,6 light tunneling, and invisible cloaking. Nanowire arrays present large aspect ratios, which lead to uniaxial anisotropy and hyperbolic dispersion, in which one direction of the material behaves like a metal and in the other direction it behaves as a dielectric.^{3,9} Hyperbolic metamaterials were first theorized and created for optical imaging beyond the diffraction limit,9 but new research has led to applications in high $T_{\rm c}$ superconductivity^{10,11} and as a potential platform for studying the fundamental physical phenomenon.^{12–15}

Much effort has been devoted toward the realization of metallic nanoarray structures for metamaterial application with techniques such as electrochemical deposition, ¹⁶ e-beam lithography, ¹⁷ and the anodic aluminum oxide (AAO) template method. ^{18,19} Although promising, the AAO template and lithography methods are typically limited by material selection, tedious multistep growth methods, and scalability. ¹⁹ It was also reported that hyperbolic dispersion and ENZ

permittivity are strongly correlated with the anisotropy and ordering of the metallic nanowire array. Thus, it is important to precisely control the metamaterials on a nanoscale for highly tunable properties. Another critical need is to produce metamaterials with hyperbolicity in shorter wavelength regimes (e.g., visible), while the demonstrated hyperbolic metamaterials are mostly in the longer wavelength regime (e.g., infrared).

Recent efforts are focused on oxide—metal hybrid metamaterials in vertically aligned nanocomposites (VANs) form, grown through a one-step pulsed laser deposition (PLD) technique. VANs have demonstrated their potential in nanoscale metamaterial design through robust material selection and highly anisotropic optical properties. The unique vertical strain coupling along the two-phase interface has led to unique multifunctionalities. However, extensive work on morphology tuning and strain engineering has been focused on oxide—oxide VAN systems and related properties. The work on strain engineering and morphology tuning in oxide—metal systems is scarce. 30,31

In this work, a new oxide-metal hybrid metamaterial (ZnO-Au) in the VAN form has been demonstrated using PLD. As illustrated in Figure 1, the Au nanopillars grow uniformly and epitaxially in the ZnO matrix. In this study, Au

Received: October 9, 2019 Accepted: January 15, 2020 Published: January 28, 2020



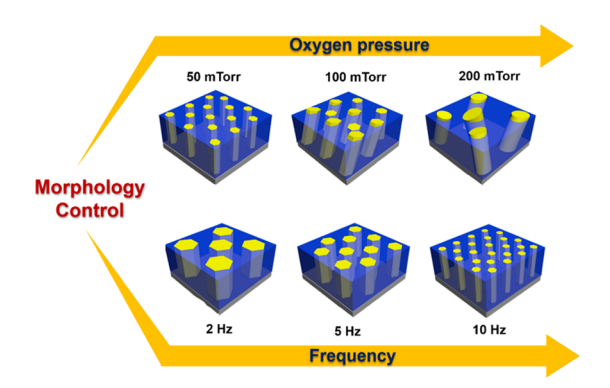


Figure 1. Schematic diagram of the ZnO–Au VAN grown on c-cut ${\rm Al_2O_3}$ and designed for optical metamaterial applications. A high degree of morphological control is possible through changing oxygen background and frequency in pulsed laser deposition.

was selected as the plasmonic metallic nanostructure in the metamaterial and ZnO was selected as the matrix due to its well-known dielectric response and piezoelectric properties. ZnO was also selected for other properties such as nontoxicity, earth abundance, and enhanced photocatalytic properties.³² The proposed morphology tuning can be achieved by varying the growth parameters such as oxygen partial pressure and laser deposition frequency. Through the morphology and inplane ordering control, it is expected to achieve tunable optical responses such as hyperbolic behavior and wavelength range, anisotropic complex dielectric properties, and plasmonic wavelength. Thus, detailed microstructural analysis including transmission electron microscopy (TEM), scanning trans-

mission electron microscopy (STEM), and energy-dispersive X-ray (EDX) mapping are conducted to couple with the optical properties measured by optical transmittance and ellipsometry.

■ RESULTS AND DISCUSSION

One of the challenges for growing a high-quality ZnO-Au VAN was the vastly different crystal structures between Au (FCC) and hexagonal ZnO (Wurtzite, HCP). This was surmounted by growing the ZnO-Au VAN on the α-Al₂O₃ substrate. There have been no reports for growth of the oxidemetal VAN in oxygen ambient due to metals hazarding a chance of oxidation upon ablation in an oxygen ambient. Oxidation was determined not to occur, as there was no presence of Au-oxide peaks in any X-ray diffraction (XRD) scans in Figure 2e or 3e or any diffraction spots besides those from Au, ZnO, or sapphire in selective area electron diffraction (SAED) patterns in Supporting Information Figure S1a,b. Interestingly, successful growth required an oxygen ambient. When growth was performed in vacuum, this led to irregular morphology and films that would easily wipe away caused by poor adhesion, possibly due to high laser plume kinetic energy. The use of a background pressure could create confinement of the plasma plume and modulation of kinetic energy, leading to more regular film growth and morphology. Formation of the ZnO-Au VAN is believed to follow a general three-step mechanism, similar to other oxide-metal VANs.²¹ A diagram of the formation mechanism can be found in Supporting Information Figure S2. Following the diagram in Supporting Information Figure S2, ZnO and Au adatoms arrive at the

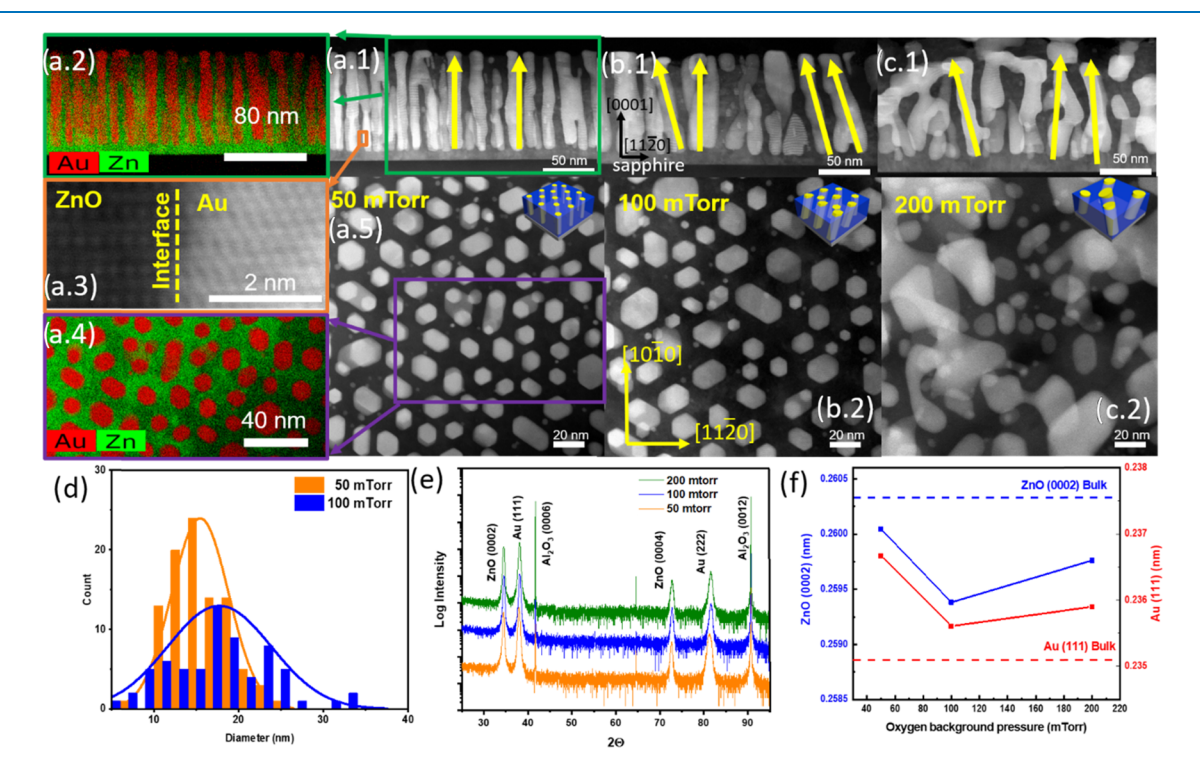


Figure 2. Oxygen background pressure study. STEM cross-section images are presented for the samples under the background pressure of (a.1) 50 mTorr, (b.1) 100 mTorr, and (c.1) 200 mTorr. Observed pillar alignment is denoted with yellow arrows in (a)–(c.1). The EDS-mapping for the 50 mTorr sample is shown for the cross-section sample in (a.2) and the plan-view sample in (a.4). HRSTEM of the ZnO–Au interface in cross-section is provided in (a.3). STEM plan-view images are shown for (a.5) 50 mTorr, (b.2) 100 mTorr, and (c.2) 200 mTorr. (d) Histogram plot of pillar diameters for the 50 and 100 mTorr samples. (e) XRD θ –2 θ scans for the samples under different oxygen pressures. (f) d-spacing calculated from (e).

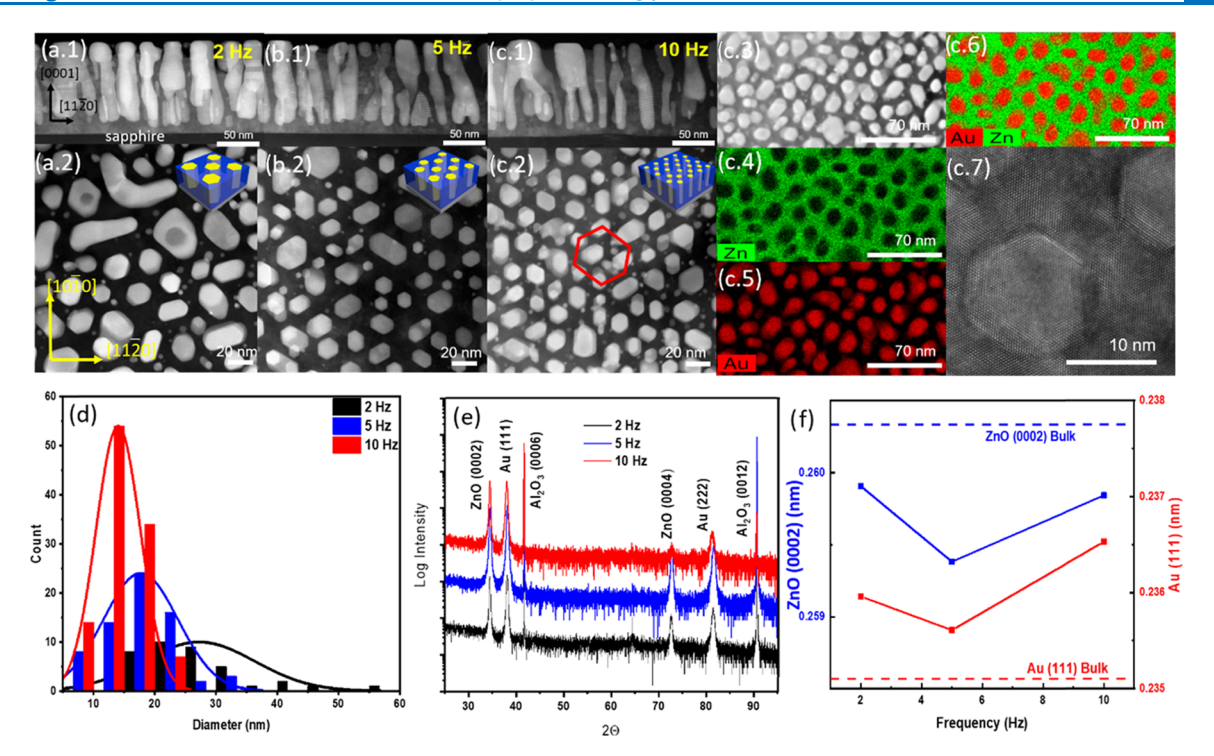


Figure 3. ZnO—Au nanocomposite samples deposited under different deposition frequencies. Cross-section STEM images shown for (a.1) 2 Hz, (b.1) 5 Hz, and (c.1) 10 Hz. Plan-view STEM images are shown for (a.2) 2 Hz, (b.2) 5 Hz, and (c.2) 10 Hz. A red hexagon is placed in (c.2) to denote quasi-hexagonal ordering. (c.3) Corresponding HAADF for EDS-mapping of 10 Hz. EDS-mapping for (c.4) Zn, (c.5) Au, and (c.6) combined. (c.7) Plan-view HRTEM of the individual Au nanopillar and the ZnO matrix obtained from the 10 Hz sample. (d) Calculated histogram of measured pillar diameters. (e) XRD study. (f) Basal plane *d*-spacing calculated from (e).

Al₂O₃ substrate and undergo surface diffusion. Second, initial nucleation begins. Owing to the different surface energies, Au nucleates as 3D islands and ZnO as 2D layers. Growth continues in this manner, with Au 3D island forming nanopillars and ZnO growing layer by layer to form the matrix. Finally, ZnO—Au forms as a pillar-in-matrix vertically aligned nanocomposite.

For optimized vertical nanopillar growth, 50 mTorr oxygen background pressure created absolute vertical growth, as seen in Figure 2a.1. The 50 mTorr film shows strong hexagonal faceted Au nanopillars arranged in hexagonal long-range order, seen in the STEM plan-view image in Figure 2a.5. The mesoscale quasi-hexagonal ordering is more obvious in the low-resolution STEM image in Supporting Information Figure 33. EDS-mapping was performed on the 50 mTorr sample in Figure 2a.2,a.4 to show there was no significant interdiffusion between Au and ZnO. To further confirm this, high-resolution STEM was performed in Figure 2a.3. This image was taken from the $\langle 10\overline{10} \rangle$ zone axis of the sapphire substrate and shows the cross-section atomic arrangement of Au and ZnO with a distinct heterointerface.

Background pressure was further increased to investigate the effect of kinetic modulation on the nanopillar morphology. Films were grown at 100 and 200 mTorr, as seen in Figure 2b.1,c.1. The average pillar diameter was calculated by measuring the diameter of pillars in STEM plan-view images in Figure 2a.5,b.2. The measured diameters were then plotted as a histogram in Figure 2d, and the average diameter was taken as the mean value of the histogram. This method is adopted from techniques used to calculate grain size distributions.^{33,34} The histogram indicates that the average pillar diameter increases from ~15 nm at 50 mTorr to ~18 nm

at 100 mTorr. For the film grown at 200 mTorr in Figure 2c.1, the cross-section image shows that nanopillars became randomly orientated and the plan-view image in Figure 2c.2 illustrates the irregular shape and loss of hexagonal ordering. In this case, the average diameter was difficult to calculate due to the irregular shape of the nanopillars. Based on STEM images coupled with the pillar diameter histogram data, the lower background pressure leads to a more uniform nanopillar distribution (Figure 2a.5), while the higher background pressure leads to a wider diameter distribution (Figure 2b.2,c.2). The pillar alignment is denoted in Figure 2a.1-c.1 with yellow arrows. Upon increasing to 100 mTorr, the nanopillar alignment appears tuned from vertical to slightly tilted. Increasing further to 200 mTorr, the pillars become more randomly orientated in the ZnO matrix. Overall, it is suggested here that lower background pressure leads to more uniform and vertically aligned pillar morphology.

X-ray diffraction was conducted to investigate the microstructure and epitaxial quality of the ZnO–Au VAN. Scans of θ – 2θ were performed for films deposited under different oxygen background pressures and shown in Figure 2e. These scans show highly textured growth with the preferred out-of-plane direction for ZnO is (0002) and for Au is (111), growing parallel with the (0006) plane of Al₂O₃. The ZnO–Au VAN was found to have an epitaxial relationship of Au(111) \parallel ZnO(0002) \parallel Al₂O₃(0006). To overcome the vastly different lattice structure, Au rotates to (111) orientation to match both the underlying substrate and the matrix. This (111) plane is the close-packed plane for the face-centered cubic lattice with 6-fold symmetry but a different plane stacking sequence compared to the structure of the ZnO matrix or the Al₂O₃ substrate. The hexagonal shape of the (111) orientation of Au

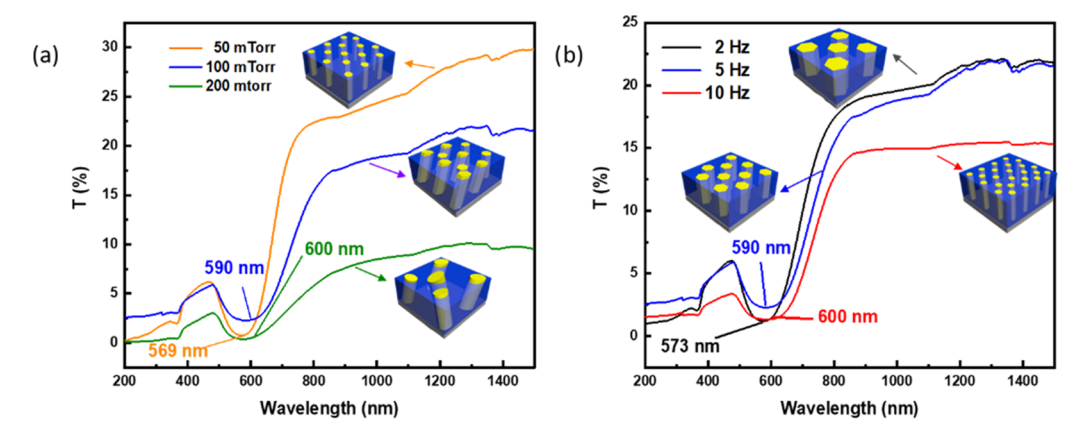


Figure 4. UV—Vis transmission (%T) spectra of the ZnO—Au VAN in the range of 200—1500 nm with changes in (a) oxygen background pressure and (b) laser frequency. Insets on each graph are models depicting each nanocomposite. The minimum in the graph represents the plasmonic response of Au and was measured and recorded for each film on the respective graph.

is also evidenced in the highly faceted Au pillar shape as seen in plan-view images. Moreover, the in-plane epitaxial relationship is determined from the plan-view SAED pattern and the cross-section SAED pattern in Supporting Information Figure S1 and found to be Au $\{220\}$ || ZnO $\{1\overline{100}\}$ || $\{1\overline{2}10\}$.

To investigate the strain states of the films, the out-of-plane d-spacing was calculated and is plotted in Figure 2f. For ZnO matrix, increasing the background pressure decreased the dspacing value from the bulk value of (0002), which indicated an increased compressive strain. For Au nanopillars, increased background caused d-spacing values to decrease toward the bulk value of (111), which indicated a decreased tensile stress. Interestingly, the tendency of the lattice parameter to decrease with the background pressure corresponded to an increased nanopillar diameter and tuned orientation. This lattice strain tuning could be related to the morphology seen in Figure 2ac. At 50 mTorr, the Au nanopillars are in a high strain state and growth is vertically aligned with both local and long-range hexagonal ordering. Au nanopillars in the 200 mTorr are in a low strain state and have random ordering with little to no hexagonal ordering. Based on the observed morphologies, the tendency of Au to grow into highly ordered, hexagonally faceted structures is believed to be driven by high strain and a desire to reduce interfacial energy with the ZnO matrix.

In parallel to tuning oxygen pressure, a set of the laser frequency study was conducted and is summarized in Figure 3. Cross-section STEM images are shown for each frequency of Figure 3(a.1) 2 Hz, (b.1) 5 Hz, and (c.1) 10 Hz. Corresponding plan-view STEM images are shown for Figure 3(a.2) 2 Hz, (b.2) 5 Hz, and (c.2) 10 Hz. A red hexagon in Figure 3c.2 in the plan-view image denotes the quasi-hexagonal in-plane ordering. EDS-mapping combined with STEM was performed on the plan-view 10 Hz sample to further show the distinct two-phase growth of Au and ZnO as seen in Figure 3c.4-6 with the corresponding HAADF appearing in Figure 3c.3. The EDS-mapping confirms the sufficiently low interdiffusion similar to that of the background pressure series. High-resolution TEM was conducted on the 10 Hz sample to demonstrate the hexagonal shape and faceted nanopillars, shown in Figure 3c.7, as well as the in-plane atomic arrangement. The six sides of the pillar are indexed as {220} family of planes.

To understand the effect of frequency on epitaxial quality and microstructure, a detailed XRD study was performed with

scans shown in Figure 3e and out-of-plane d-spacing values were calculated in Figure 3f. The average diameters were calculated by a similar method as highlighted above and plotted as a histogram in Figure 3d. The films grown had diameters of 27, 18, and 15 nm for deposition at 2, 5, and 10 Hz, respectively. As the frequency is increased, statistically the diameter of Au nanopillars is decreased. This is observed from plan-view STEM images in Figure 3a.2-c.2. It is suggested here that increasing the pulse frequency will shorten the diffusion length of impinged adatoms. The increased frequency will impede the ability of adatoms to reach thermodynamic equilibrium, creating disorder and strain in the film. This is observed with XRD scans in Figure 3e and the calculated dspacing in Figure 3f. For the 2 Hz film, ZnO d-spacing is close to the bulk value of (0002), but as the frequency is increased to 5 and 10 Hz, the *d*-spacing decreases, indicating an increase in compressive stress. Conversely, the *d*-spacing of (111) Au at 2 Hz is greater than the bulk value and gradually increases with frequency, indicating an increase in the out-of-plane tension of nanopillars.

The advantage of the film grown in this report is the inherent anisotropy and strain engineering, which leads to hyperbolic dispersion and epsilon near-zero permittivity. Strong plasmonic resonance is expected at the ZnO/Au interface, making the ZnO-Au hybrid material useful for different types of gas sensors and energy harvesting.^{35,36} Due to the excellent epitaxial quality, as seen in XRD scans above for the deposited ZnO-Au VAN, the optical properties are expected to be enhanced as compared with other metallic nanowire arrays and ZnO-Au nanocomposites. To directly observe plasmonic resonance of the ZnO-Au VAN, UV-vis transmittance spectra were obtained. The results of the films deposited at different background pressures are shown in Figure 4a, and those for a different laser frequency are shown in Figure 4b. There is an obvious surface plasmon resonance (SPR) caused by Au in the transmittance spectra, occurring at around 600 nm. The red shift of the plasmon resonance in the case of background pressure spectra in Figure 4a correlates with the randomization of nanopillar orientation and caused by a broadening of the absorption edge. The transmission (T%)overall decreases for films at a higher background pressure, possibly due to more light being scattered and absorbed by the film because of an increased pillar size and changed orientation. Optical band gap values were calculated via a

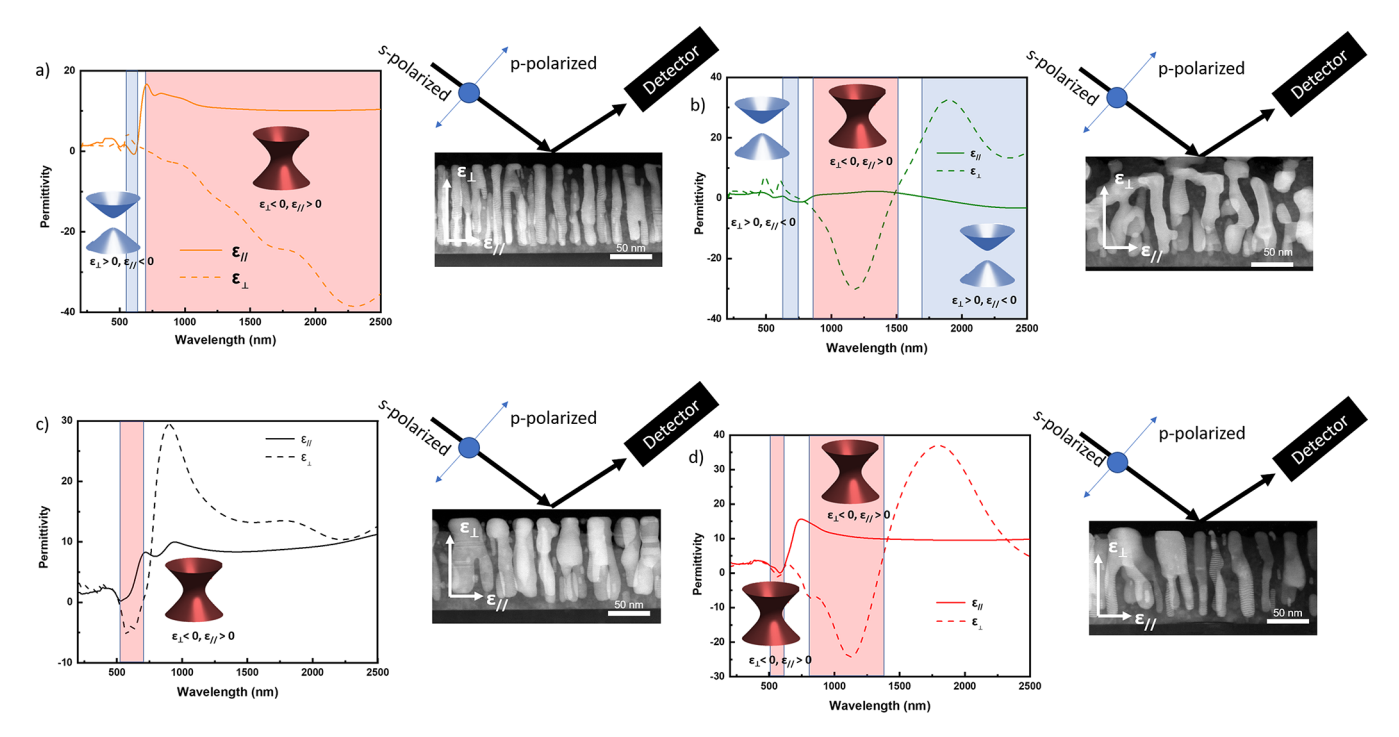


Figure 5. Real parts of $\varepsilon \parallel$ and $\varepsilon \perp$ are graphed for (a) 50 mTorr, (b) 200 mTorr, (c) 2 Hz, and (d) 10 Hz. Regimes of hyperbolicity are marked on the graphs in both red and blue, corresponding to the respective isofrequency curves of either a hyperboloid of two sheets (blue) or a hyperboloid of one sheet (red). The polarization of the beam experiment with respect to the microstructure of each film is shown in (a), (b), (c), and (d). The parallel and perpendicular directions of permittivity are marked on the cross-section STEM image.

Tauc method to investigate the effect Au inclusion had on the ZnO optical band gap. The band gaps calculated for oxygen pressure are shown in Supporting Information Figure S4a. There is no obvious trend in the optical band gap tuning with respect to background pressure tuning.

Transmission spectra were also obtained for films deposited at a different laser pulse frequency and are presented in Figure 4b. There is a plasmon resonance dip occurring at around 600 nm due to the Au nanopillars. The absorption edge slightly broadens as the frequency is increased, possibly due to an increased number of Au nanopillars. The surface plasmon minima also broaden with the increasing background pressure, possibly caused by a higher level of strain. Optical band gaps were calculated for frequency variation films and are plotted in Supporting Information Figure S4b. As frequency increases, the optical band gap decreases. The ZnO-Au film deposited at 10 Hz has a higher density of pillars than the film deposited at 2 Hz. A higher density of pillars could create more interfaces, increasing the amount of light that is scattered and decreasing the optical band gap.

The hyperbolic properties observed in optical metamaterials are a direct result of the isofrequency surface of extraordinary waves, which is given by the following formula⁴

$$\frac{k_x^2 + k_y^2}{\varepsilon_{||}} + \frac{k_z^2}{\varepsilon_{\perp}} = \left(\frac{\omega}{c}\right)^2$$

The hyperbolic dispersion and ENZ permittivity of the ZnO-Au VAN were investigated through spectroscopic ellipsometry. The real part of the dielectric function, related to the permittivity of the film, is presented in Figure 5. Representative isofrequency curves, which determine the photonic density of states that can be supported within the material, are shown in each graph. The regions are color-coded to their corresponding

surface of either a hyperboloid of two sheets (blue shaded color) or a hyperboloid of one sheet (red shaded color). Data was measured from 210 to 2500 nm at three different angles of 30, 45, and 60°. The data were fitted with a uniaxial model to discern the in-plane and out-of-plane components of the dielectric function. A B-spline model was used on both inplane and out-of-plane, and a reasonable mean square error (MSE) <5 occurred for all films. Ellipsometry parameters psi and delta are shown in the Supporting Information. The anisotropy axis is shown for each experimental setup in (a), (b), (c), and (d) with subscripts \parallel and \perp indicating, respectively, the components parallel (in-plane) and perpendicular (out-of-plane) to the anisotropy axis.

The ZnO-Au films grown in this work all have hyperbolic dispersion and ENZ points across many different ranges, but most interestingly, they all have it in the shorter wavelength (visible) regime. The permittivity of the film deposited at 50 mTorr is shown in Figure 5a, and the permittivity of the 200 mTorr film is shown in Figure 5b. The film grown at 50 mTorr shows hyperbolic dispersion in the visible spectrum and in the near-infrared regime up to the far end of the measured spectrum. In the 50 mTorr film, ε_{\parallel} (in-plane component) behaves mostly as a dielectric material except for in the visible regime from around 500 to 700 nm, where ε_{\parallel} is driven negative, caused by the surface plasmon resonance. The perpendicular component ε_{\perp} (out-of-plane) has a permittivity with strictly metallic behavior. The 50 mTorr film in the visible regime has hyperbolic dispersion with an isofrequency surface of a hyperboloid of two sheets (blue shaded color), and in the near-infrared regime, the surface is tuned to become a hyperboloid of one sheet (red shaded color). The 50 mTorr film also has three ENZ points, two in the parallel direction in the visible regime at 520 and 625 nm and the perpendicular component has one ENZ point in the visible regime at 715 nm. The hyperbolic properties of the 50 mTorr film correlate well with the overall hexagonal ordered, vertically aligned morphology. Vertically aligned Au metallic nanopillars cause the perpendicular permittivity to be negative, and the ZnO dielectric media is expressed in the parallel component having positive permittivity. When Au nanopillar morphology is tuned by growth at 200 mTorr to be randomly arranged in Figure 5b, this leads to an increased number of epsilon near-zero (ENZ) points in the visible and infrared spectra. The parallel component has ENZ points of 657, 835, and 1762 nm, while the perpendicular component has ENZ points at 744 and 1468 nm. It is also possible to change the hyperbolic isofrequency surface in the long range (above 1500 nm) from a hyperboloid of one sheet in the 50 mTorr film to a hyperboloid of two sheets in the 200 mTorr film. The 200 mTorr film has an interesting parallel component with almost near-zero permittivity for the entire measured spectrum regime. It oscillates between being slightly negative and slightly positive while crossing zero permittivity at three different points, though it never has a permittivity outside of ± 3 . A material with epsilon near-zero permittivity and hyperbolic dispersion across a broad-spectrum range is of particular interest for subdiffraction imaging or other hyperbolic metamaterial application.³

The effect of frequency tuning on hyperbolic dispersion was also investigated. The permittivity of the film grown at 2 Hz is shown in Figure 5c, in which the film only has a small hyperbolic regime in the visible spectrum and the perpendicular component has ENZ points at 515 and 697 nm. Upon increasing laser frequency, the number of ENZ points increases and the film demonstrates hyperbolic dispersion in the near infrared. The perpendicular component has ENZ points at 542, 595, 716, and 1348 nm. Tuning pulse laser deposition frequency changes the size and number of hyperbolic regimes, but it does not tune the overall isofrequency surface geometry. As compared with the background pressure series of films, the pulse laser frequency series does not have as good of hyperbolic properties, but the series does have significant epsilon near-zero permittivity points.

Parallel systematic tuning experiments of pulsed laser frequency and oxygen background pressure were designed to investigate the effect on strain states and morphology in the ZnO-Au VAN structure, as per Figure 1. Frequency dependence was selected as one of the studies because it is well-known to affect the oxide-metal VAN diameter,³⁰ where the diameter of nanowires has been highly correlated with optical properties.³⁸ Conversely, background pressure was studied because its effect on the oxide-metal VAN has not yet been studied. Individual Au nanopillars in the matrix grown at high strain states were shown to have beautiful, faceted, hexagonal structure and long-range quasi-hexagonal in-plane order. Of the two series of films of oxygen background pressure and laser frequency, each series demonstrated an ability to tune the hyperbolic properties of the films in unique ways. There are a few key conclusions that can be surmised when considering the background pressure series and the pulse laser frequency series. Overall, the background pressure series shows broader hyperbolic properties in both shorter and longer wavelengths compared with the pulse laser frequency series, which is ideal for tunable hyperbolic metamaterial application. Changing the background pressure from 50 to 200 mTorr allows the isofrequency surface to be tuned. The easily controllable isofrequency curve in the visible and infrared regimes is something not previously demonstrated. Manipulating the isofrequency surface is important because it is useful in an application for focusing in hyperlenses and subdiffraction imaging.³⁹ In the pulse laser frequency series, by changing the deposition frequency from 2 to 10 Hz, this created a hyperbolic regime in the infrared and increased the number of epsilon near-zero permittivity points. Overall, the background pressure series demonstrated superior hyperbolic metamaterial properties and wider application when compared with the pulse laser frequency series. The key issue facing the hyperbolic metamaterial in their application includes small hyperbolic regimes, controllability, and lack of properties in visible regimes. The background pressure series solves most of these key issues; it demonstrates broad hyperbolicity in both short and long wavelengths, and through manipulation of morphology and the quasi-hexagonal in-plane ordering in these films, it is possible to easily control metamaterial properties.

CONCLUSIONS

Two-phase ZnO-Au VAN films have been grown through a simple, self-assembly one-step PLD method. ZnO-Au nanocomposites morphology demonstrated beautiful, vertically aligned Au pillars with quasi-hexagonal in-plane ordering that were embedded in a ZnO matrix. The effect of PLD parameters on film morphology and strain was investigated through different experimental growth series, an oxygen background pressure series, and a pulse laser frequency series. Background pressure showed an ability to tune the orientation and ordering of the Au nanopillars, while pulse frequency was able to tune the size of pillars. High strain states lead to a small pillar size and a high degree of quasi-hexagonal in-plane ordering, while low strain states induce decreased ordering and a large pillar size. The ZnO-Au VAN due to its anisotropy and strain-driven hexagonal-closed packed ordering demonstrates interesting hyperbolic dispersion and epsilon near-zero (ENZ) permittivity in both the visible and near-infrared regimes. Plasmonic properties are shown to be easily controlled through morphology. As well, the ZnO-Au VAN was found to have excellent epitaxial quality, lending to enhanced optical properties, potential energy, and sensor application. Future work will focus on the application of the ZnO-Au VAN in the sensor and metamaterial technologies.

EXPERIMENTAL SECTION

Thin-Film Growth. ZnO-Au vertically aligned nanocomposite films were grown through pulsed laser deposition on c-cut Al₂O₃ (0001) in two series, an oxygen background pressure series and a pulse laser frequency series. Across all series, deposition was performed with a KrF excimer laser (Lambda Physik Complex Pro 205, λ = 248 nm), and the substrate temperature was kept constant at 500 °C. The laser beam was focused with an incident angle of 45° with a laser energy of 420 mJ. The target-substrate distance was kept constant at 4.5 cm and measured before each deposition to ensure accuracy. A nanocomposite target composed of 1:1 Au/ ZnO developed through solid-state sintering was used for laser ablation. Before deposition, the chamber was pumped down to around 10⁻⁶ mTorr before an oxygen pressure was inflowed. For the background pressure series, deposition occurred from 50 to 200 mTorr with a constant pulse frequency of 5 Hz. The pulse laser frequency series maintained a constant pressure of 100 mTorr, while laser frequency repetition was varied from 2 to 10 Hz. The reference sample between the two series was

deposited at 5 Hz and 100 mTorr. After all depositions, the chamber was cooled to room temperature at a rate of 15 $^{\circ}$ C/min.

Microstructure Characterization. Film morphology was characterized through XRD, TEM, and STEM coupled with EDS-mapping. XRD scans of θ –2 θ were conducted using a Panalytical X'Pert X-ray diffractometer with Cu Kα radiation. Bright-field TEM, STEM, SAED patterns, and EDS-mapping were performed in an FEI Talos F200X TEM. Samples for electron microscopy were prepared, for both cross-section and plan-view, via a standard grinding procedure, which entails manual grinding, polishing, dimpling, and a final ion milling step to achieve electron transparency (PIPS 691 precision ion polishing system, 5 keV for the cross-section sample, and 4–4.5 keV for the plan-view sample).

Optical Measurements. Ellipsometry experiments were carried out on an RC2 spectroscopic ellipsometer (J.A. Woollam Company). Three angles 30, 45, and 60° were measured from a spectrum range of 210–2500 nm. Psi and delta data obtained from ellipsometry experiments and then fit with a uniaxial model coupled with the B-spline model were used to discern anisotropic permittivity properties of the ZnO–Au VAN, and an agreeable mean square error (MSE) <5 was obtained for all film models. Normal incident depolarized transmittance (*T*%) was measured using an optical spectrophotometer (Lambda 1050 UV–vis spectrophotometer).

ASSOCIATED CONTENT

Supporting Information

The Supporting Information is available free of charge at https://pubs.acs.org/doi/10.1021/acsomega.9b03356.

Indexed SAED pattern for ZnO–Au cross-section and plan-view, STEM image showing broader in-plane ordering, optical band gap calculation for ZnO, spectroscopic ellipsometry measured and model data for ψ and Δ (PDF)

AUTHOR INFORMATION

Corresponding Author

Haiyan Wang — School of Materials Engineering and School of Electrical and Computer Engineering, Purdue University, West Lafayette, Indiana 47907, United States; ocid.org/0000-0002-7397-1209; Email: hwang00@purdue.edu

Authors

Robynne L. Paldi — School of Materials Engineering, Purdue University, West Lafayette, Indiana 47907, United States Xing Sun — School of Materials Engineering, Purdue University,

Xuejing Wang — School of Materials Engineering, Purdue University, West Lafayette, Indiana 47907, United States

Xinghang Zhang – School of Materials Engineering, Purdue University, West Lafayette, Indiana 47907, United States

Complete contact information is available at: https://pubs.acs.org/10.1021/acsomega.9b03356

West Lafayette, Indiana 47907, United States

Author Contributions

The project was conceived and led by H.W. R.L.P. deposited the films and conducted the property measurements. X.W. and R.L.P. conducted the optical measurement and analysis. X.S. and R.L.P. prepared the TEM samples and conducted the TEM study. L.L. prepared the target. The manuscript was

drafted and revised by R.L.P., H.W., and X.Z., and all authors have revised and given the approval for the final version of the manuscript.

Notes

The authors declare no competing financial interest.

ACKNOWLEDGMENTS

This work was supported by the U.S. Department of Energy, Office of Science, Basic Energy Sciences under Award DE-SC0020077. R.L.P. acknowledges the funding support from the Purdue Doctoral Fellow program. X.W. and X.S. acknowledge the support from U.S. National Science Foundation (DMR-1565822) for the TEM characterization effort.

REFERENCES

- (1) Garcia, N.; Ponizowskaya, E. V.; Zhu, H.; Xiao, J. Q.; Pons, A. Wide photonic band Gaps at the visible in metallic nanowire arrays embedded in a dielectric matrix. *Appl. Phys. Lett.* **2003**, *82*, 3147–3149.
- (2) Garcia, N.; Ponizovskaya, E. V.; Xiao, J. Q. Zero Permittivity materials: band gaps at the visible. *Appl. Phys. Lett.* **2002**, *80*, 1120–1122.
- (3) Ferrari, L.; Wu, C.; Lepage, D.; Zhang, X.; Liu, Z. Hyperbolic metamaterials and their applications. *Prog. Quantum Electron.* **2015**, 40, 1–40.
- (4) Poddubny, A.; Iorsh, I.; Belov, P.; Kivshar, Y. Hyperbolic metamaterials. *Nat. Photonics* **2013**, *7*, 948–957.
- (5) Silveirinha, M.; Engheta, N. Tunneling of electromagnetic energy through subwavelength channels and bends using ε -near-zero materials. *Phys. Rev. Lett.* **2006**, 97, 1–4.
- (6) Adams, D. C.; Inampudi, S.; Ribaudo, T.; Slocum, D.; Vangala, S.; Kuhta, N. A.; Goodhue, W. D.; Podolskiy, V. A.; Wasserman, D. Funneling light through a subwavelength aperture with epsilon-near-zero materials. *Phys. Rev. Lett.* **2011**, *107*, 1–5.
- (7) Liu, R.; Cheng, Q.; Hand, T.; Mock, J. J.; Cui, T. J.; Cummer, S. A.; Smith, D. R. Experimental demonstration of electromagnetic tunneling through an epsilon-near-zero metamaterial at microwave frequencies. *Phys. Rev. Lett.* **2008**, *100*, 1–4.
- (8) Hao, J.; Yan, W.; Qiu, M. Super-reflection and cloaking based on zero index metamaterial. *Appl. Phys. Lett.* **2010**, *96*, No. 101109.
- (9) Jacob, Z.; Alekseyev, L. V.; Narimanov, E. Optical Hyperlens: Far-field imaging beyond the diffraction limit. *Opt. Express* **2006**, *14*, No. 8247
- (10) Smolyaninov, I. I.; Smolyaninova, V. N. Is there a metamaterial route to high temperature superconductivity? *Adv. Condens. Matter Phys.* **2014**, 2014, No. 479635.
- (11) Smolyaninov, I. I. Quantum topological transition in hyperbolic metamaterials based on high Tc superconductors. *J. Phys. Condens. Matter* **2014**, *26*, No. 305701.
- (12) Smolyaninov, I. I. Analog of gravitational force in hyperbolic metamaterials. *Phys. Rev. A: At., Mol., Opt. Phys.* **2013**, 88, No. 033843.
- (13) Smolyaninov, I. I. Modeling of causality with metamaterials. J. Opt. 2013, 15, 1591–1595.
- (14) Smolyaninov, I. I.; Hwang, E.; Narimanov, E. Hyperbolic metamaterial interfaces: hawking radiation from rindler horizons and spacetime signature transitions. *Phys. Rev. B: Condens. Matter Mater. Phys.* **2012**, *85*, 1–7.
- (15) Smolyaninov, I. I.; Yost, B.; Bates, E.; Smolyaninova, V. N. Experimental demonstration of metamaterial "multiverse" in a ferrofluid. *Opt. Express* **2013**, *21*, 14918.
- (16) Kabashin, A. V.; Evans, P.; Pastkovsky, S.; Hendren, W.; Wurtz, G. A.; Atkinson, R.; Pollard, R.; Podolskiy, V. A.; Zayats, A. V. Plasmonic nanorod metamaterials for biosensing. *Nat. Mater.* **2009**, *8*, 867–871.

- (17) Melosh, N. A.; Boukai, A.; Diana, F.; Gerardot, B.; Badolato, A.; Petroff, P. M.; Heath, J. R. Ultrahigh-density nanowire lattices and circuits. *Science* **2003**, *300*, 112–115.
- (18) Shukla, S.; Kim, K. T.; Baev, A.; Yoon, Y. K.; Litchinitser, N. M.; Prasad, P. N. Fabrication and characterization of gold-polymer nanocomposite plasmonic nanoarrays in a porous alumina template. *ACS Nano* **2010**, *4*, 2249–2255.
- (19) Stępniowski, W. J.; Salerno, M. Fabrication of nanowires and nanotubes by anodic Alumina template-assisted electrodeposition. *Manufacturing Nanostructures*; One Central Press, 2014; pp 321–357.
- (20) Misra, S.; Li, L.; Jian, J.; Huang, J.; Wang, X.; Zemlyanov, D.; Jang, J.; Ribeiro, F. H.; Wang, H. Tailorable Au nanoparticles embedded in epitaxial TiO2 thin films for tunable optical properties. *ACS Appl. Mater. Interfaces* **2018**, *10*, 32895–32902.
- (21) Li, L.; Sun, L.; Gomez-Diaz, J. S.; Hogan, N. L.; Lu, P.; Khatkhatay, F.; Zhang, W.; Jian, J.; Huang, J.; Su, Q.; et al. Self-assembled epitaxial Au-oxide vertically aligned nanocomposites for nanoscale metamaterials. *Nano Lett.* **2016**, *16*, 3936–3943.
- (22) Sun, X.; Li, Q.; Huang, J.; Jian, J.; Lu, P.; Zhang, X.; Macmanus-Driscoll, J. L.; Wang, H. Strain and property tuning of the 3D framed epitaxial nanocomposite thin films via interlayer thickness variation. *J. Appl. Phys.* **2019**, *125*, No. 082530.
- (23) Gao, X.; Li, L.; Jian, J.; Wang, H.; Fan, M.; Huang, J.; Wang, X.; Wang, H. Vertically Aligned Nanocomposite BaTiO3:YMnO3 Thin films with room temperature multiferroic properties toward nanoscale memory devices. ACS Appl. Nano Mater. 2018, 1, 2509–2514.
- (24) Chen, A.; Bi, Z.; Jia, Q.; Macmanus-Driscoll, J. L.; Wang, H. Microstructure, vertical Strain control and tunable functionalities in self-Assembled, vertically aligned nanocomposite thin films. *Acta Mater.* **2013**, *61*, 2783–2792.
- (25) Wang, X.; Jian, J.; Zhou, Z.; Fan, C.; Dai, Y.; Li, L.; Huang, J.; Sun, J.; Donohue, A.; Bermel, P.; et al. Self-assembled Ag—TiN hybrid plasmonic metamaterial: tailorable tilted nanopillar and optical properties. *Adv. Opt. Mater.* **2019**, *7*, No. 1801180.
- (26) Huang, J.; Wang, X.; Hogan, N. L.; Wu, S.; Lu, P.; Fan, Z.; Dai, Y.; Zeng, B.; Starko-Bowes, R.; Jian, J. et al. Nanoscale artificial plasmonic lattice in self-assembled vertically aligned nitride—metal hybrid metamaterials. *Adv. Sci. 5*, 1800416. DOI: 10.1002/advs.201800416.
- (27) Sun, X.; Huang, J.; Jian, J.; Fan, M.; Wang, H.; Li, Q.; Mac Manus-Driscoll, J. L.; Lu, P.; Zhang, X.; Wang, H. Three-dimensional strain engineering in epitaxial vertically aligned nanocomposite thin films with tunable magnetotransport properties. *Mater. Horiz.* **2018**, *5*, 536–544.
- (28) Fan, M.; Wang, H.; Misra, S.; Zhang, B.; Qi, Z.; Sun, X.; Huang, J.; Wang, H. Microstructure, magnetic, and magnetoresistance properties of La0.7Sr0.3MnO3:CuO nanocomposite thin films. *ACS Appl. Mater. Interfaces* **2018**, *10*, 5779–5784.
- (29) Sun, X.; Li, Q.; Huang, J.; Fan, M.; Rutherford, B. X.; Paldi, R. L.; Jian, J.; Zhang, X.; Wang, H. Strain-driven nanodumbbell structure and enhanced physical properties in hybrid vertically aligned nanocomposite thin films. *Appl. Mater. Today* **2019**, *16*, 204–212.
- (30) Huang, J.; Li, L.; Lu, P.; Qi, Z.; Sun, X.; Zhang, X.; Wang, H. Self-assembled Co-BaZrO3 nanocomposite thin films with ultra-fine vertically aligned Co nanopillars. *Nanoscale* **2017**, *9*, 7970–7976.
- (31) Zhang, B.; Fan, M.; Li, L.; Jian, J.; Huang, J.; Wang, H.; Kalaswad, M.; Wang, H. Tunable magnetic anisotropy of self-assembled Fe nanostructures within a La0.5Sr0.5FeO3 matrix. *Appl. Phys. Lett.* **2018**, *112*, No. 013104.
- (32) Chen, X.; Wu, Z.; Liu, D.; Gao, Z. Preparation of ZnO photocatalyst for the efficient and rapid photocatalytic degradation of Azo dyes. *Nanoscale Res. Lett.* **2017**, *12*, No. 143.
- (33) Mendelson, M. I. Average grain size in polycrystalline ceramics. *J. Am. Ceram. Soc.* **1969**, *52*, 443–446.
- (34) Chakraverty, B. K. Grain size distribution in thin films. *J. Phys. Chem. Solids* **1967**, 28, 2401–2412.
- (35) Zhou, F.; Wang, Q.; Liu, W. Au@ZnO nanostructures on porous silicon for photocatalysis and gas-sensing: the effect of

- plasmonic hot-electrons driven by visiblelight. *Mater. Res. Express* **2016**, 3, No. 085006.
- (36) Gaiardo, A.; Fabbri, B.; Giberti, A.; Guidi, V.; Bellutti, P.; Malagù, C.; Valt, M.; et al. Chemical ZnO and Au / ZnO thin films: room-temperature chemoresistive properties for gas sensing applications. Sens. Actuators, B 2016, 237, 1085–1094.
- (37) Maas, R.; Parsons, J.; Engheta, N.; Polman, A. Experimental realization of an epsilon-near-zero metamaterial at visible wavelengths. *Nat. Photonics* **2013**, *7*, 907–912.
- (38) Starko-Bowes, R.; Atkinson, J.; Newman, W.; Hu, H.; Kallos, T.; Palikaras, G.; Fedosejevs, R.; Pramanik, S.; Jacob, Z. Optical characterization of epsilon-near-zero, epsilon-near-pole, and hyperbolic response in nanowire metamaterials. *J. Opt. Soc. Am. B* **2015**, 32, No. 2074.
- (39) Macêdo, R.; Dumelow, T.; Stamps, R. L. Tunable focusing in natural hyperbolic magnetic media. *ACS Photonics* **2016**, *3*, 1670–1677.